

## A triple-exposure color PIV technique for pressure reconstruction

WANG ZhongYi, GAO Qi\* & WANG JinJun

*Key Laboratory of Fluid Mechanics, Ministry of Education, Beijing University of Aeronautics and Astronautics, Beijing 100191, China*

Received April 7, 2016; accepted July 8, 2016; published online December 21, 2016

The study developed a triple-exposure color particle image velocimetry (TE-CPIV) technique associated with pressure reconstruction, and validated its feasibility. A light source with the three primary colors of red, green, and blue ( $R$ ,  $G$ , and  $B$ ) is produced in a time sequence by a liquid crystal display (LCD) projector. Particle images at three different instants under the color illuminations are captured in one snapshot using a color digital single-lens reflex (SLR) camera with a complementary metal-oxide semiconductor (CMOS) sensor. A contamination correction algorithm based on a specific calibration is performed on the different color layers ( $R$  layer,  $G$  layer, and  $B$  layer) of the raw color image to reduce the contaminated intensity of each color illumination on the other two color layers. The corrected intensity generates three new color layers, from which a standard cross-correlation process in the classical PIV method is used to obtain two velocity fields. Eventually, an instantaneous pressure field is reconstructed from the two velocity fields. The feasibility of TE-CPIV was tested by two experiments with a solid body rotation flow and a cylinder wake flow. The results show acceptable accuracy and robustness of the new technique. The idea of the TE-CPIV is believed to provide a simple and effective way of estimating a pressure field with low cost and high convenience.

### triple exposures, color PIV, pressure reconstruction

**Citation:** Wang Z Y, Gao Q, Wang J J. A triple-exposure color PIV technique for pressure reconstruction. *Sci China Tech Sci*, 2017, 60: 1–15, doi: 10.1007/s11431-016-0270-x

## 1 Introduction

Particle image velocimetry (PIV) is an optical technique for velocity measurement. With laser illumination modulated into a sheet or volume light source, velocity on a two-dimensional plane or in a three-dimensional volume can be obtained by tracking tracer particles seeded in the flow field. In addition to the processing algorithm, the velocity quality depends mainly on the imaging system. One of the main hardware elements in PIV, the imaging camera, has been developed rapidly in recent years, especially for high-speed imaging systems. Therefore, time-resolved velocity with a high spatial resolution can be acquired by a high-speed camera. Recently, researchers have paid increasing attention

to dynamic characteristics such as pressure and force in fluid mechanics, and not only to kinetic characteristics such as velocity [1]. With access to time-resolved velocity, pressure reconstruction by solving the Navier-Stokes (N-S) equation becomes achievable. However, obtaining time-resolved velocity using high speed cameras is normally very expensive.

Many researchers have been trying to find alternative ways to achieve pressure measurement with low cost. One of these ways uses a multiple-exposure imaging system; in particular, a triple-exposure imaging system, because at least three particle images are necessary to reconstruct a pressure field. Sridhar and Katz [2] measured velocity and material acceleration using a triple-exposure imaging method. Chang [3] applied a multiple-pulsed particle tracking velocimetry (PTV) method with double exposures

\*Corresponding author (email: qigao@buaa.edu.cn)

in the first image and a single exposure in the second image to realize acceleration measurement. Liu and Katz [4] reconstructed an instantaneous pressure field with a four-exposure PIV system.

Beyond the normal multiple-exposure PIV system, Jaw et al. [5] developed an alternating-color micro-PIV system with triple-exposure imaging to acquire acceleration distribution of micro flow. This kind of color PIV is a novel approach for velocity determination, which could provide more information of the flow field compared with classical PIV [6]. Instead of using a laser with a single color as the light source, color PIV adopts a light source with multiple colors, which requires a color camera for imaging. Different colors can signify additional characteristics of the flow.

The color PIV technique has been studied extensively. Most researchers used spatially distributed color illumination to acquire velocity with more components and dimensions [7–9]. Cenedese and Paglialunga [10] utilized two parallel light sheets with different colors in depth and developed a color PIV technique similar to dual-plane PIV to acquire two-dimensional, three-component (2D3C) velocity. Pick and Lehmann [11] developed a multiple-color-plane PIV technique similar to stereoscopic-PIV (SPIV) to realize 3D3C velocity measurement. Brücker [12] produced different-colored light sheets along the depth direction of a volume domain and obtained a 3D3C velocity field. Murai et al. [13] produced a light source with three colors varying in the depth direction and acquired a 3D3C velocity field using a single high-speed video camera. Instead of using color to represent the spatial information, researchers have also tried to use color to signify temporal information [5]. Cenedese and Romano [14] developed a color-coded PTV method. Particles were illuminated by blue and green light illuminations at different instants during which a red light was used to illuminate the flow domain. Then, by tracking particles, the displacement and velocity could be obtained. Funatani et al. [15] used a color digital single-lens reflex (SLR) camera with CMOS sensor to capture particle images under three color light illuminations and improved the spatial and temporal resolution. Jaw et al. [16,17] developed an alternating color image anemometry (ACIA) method. They recorded alternating color, multi-exposure particle images with a 3-CCD color camera and then analyzed the multi-exposure image after separating different color sequential images (a blue exposure and a green exposure).

Unfortunately, the issue of color contamination during separation of different color layers was normally not considered until very recently [5,6,13,18]. Furthermore, most researchers considered the contaminated intensity to have a first-order linear relationship with the intensity of the illumination when reducing color contamination, without specific calibration of the imaging system characteristics or performing the calibration on uncompressed images of a raw format [19]. Furthermore, dynamic quantities such as pressure have rarely been touched or benefited from color

PIV techniques.

Because color PIV can provide more information than classical PIV, we associate color with time information and successfully reconstruct a pressure field based on velocity from a color PIV measurement. A triple-exposure color PIV (TE-CPIV) system is designed using the most accessible commercial devices of a liquid crystal display (LCD) projector as a light source and a color single-lens reflex (SLR) camera with a complementary metal-oxide semiconductor (CMOS) sensor as a recorder for velocity-pressure measurement. Specific contamination correction with an idea similar to that of Murai et al. [13] is applied to correct the intensity of the experimental image for accurate velocity determination. Two consecutive velocity fields can be acquired by applying a standard PIV correlation procedure to TE-CPIV, and they can be processed further to reconstruct pressure. The feasibility of the technique for pressure reconstruction is validated through experiments of a rotating solid body flow and a cylinder wake flow. Although only 2D plane velocity is discussed in the current work, the new technique can potentially be applied in 3D flow measurement with more color cameras. The cheap and easily accessible devices make this technique convenient for researchers to use.

## 2 Methodology

The TE-CPIV system developed in the present work consists of an LCD projector to produce three pulses of color illumination ( $R$ ,  $G$ , and  $B$ ) and a color SLR camera to record particle images. The principle and operating procedures are described in this section. Figure 1 shows the principle of the TE-CPIV technique for pressure reconstruction, which is divided into four procedures as follows:

Step 1 Acquire experimental raw images with a color SLR camera to capture particle images in one exposure under triple color illumination ( $R$ ,  $G$ , and  $B$ ) produced from an LCD projector (Section 2.1).

Step 2 Acquire calibration raw images under each single pure color illumination to detect the corresponding calibration function for contamination correction on each color layer (Section 2.1).

Step 3 Perform contamination correction on the basis of a set of correction equations (by combining calibration functions) to reduce the inherent color contamination of the camera system, and use the corrected intensity to generate three new color layers (Section 2.2).

Step 4 Calculate two velocity fields through a standard PIV processing algorithm from the three new color layers and eventually reconstruct the pressure field from the velocity fields (Section 2.3).

As shown in Figure 1, particle images are recorded in one exposure under different color illuminations during the experiment. Therefore, a three-color pattern for an individual

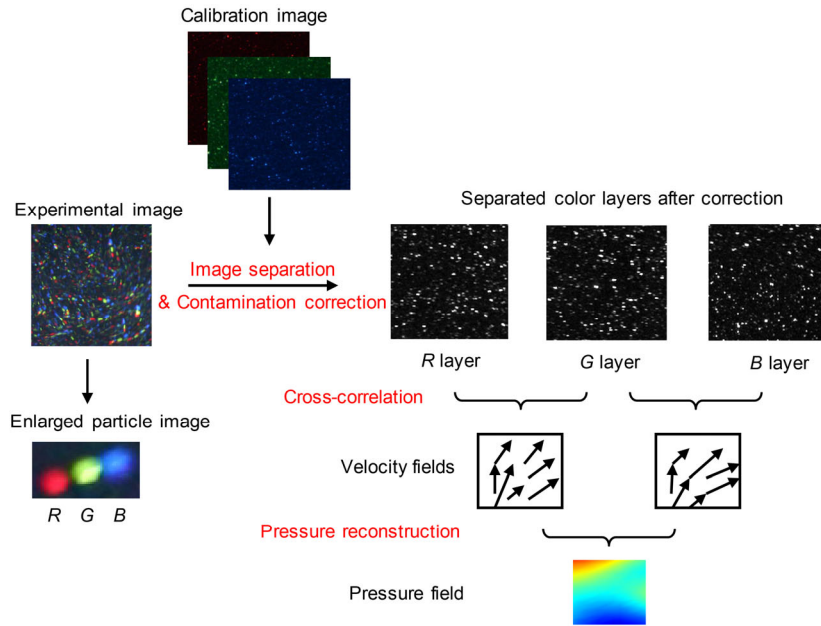


**Figure 1** (Color online) Principle of TE-CPIV for pressure reconstruction.

tracer particle is produced, as the enlarged particle image shows. After taking the experimental images, a calibration is conducted. It should be noted that the calibration for color contamination is not the traditional PIV calibration for the magnification factor (or mapping function for SPIV or volumetric PIV), but a calibration for color recording characteristics. To maintain the same imaging characteristics of the recording system as in the experimental process, the same particle field in the experiment is recorded as a calibration image. Because the color recording characteristics can cause an inescapable issue of color contamination in color PIV, a simple algorithm is executed in this study on the basis of the calibration images to reduce the color contamination and correct the recorded intensity on different color layers of the raw experimental images. The process of color contamination reduction is described in detail in Section 2.2. The corrected intensity for each color image can generate three new color layers as shown in Figure 1: the *R* layer, *G* layer, and *B* layer. Velocity and pressure fields can eventually be deduced from the separated color layers.

## 2.1 Imaging time sequence

In the TE-CPIV technique, two types of raw images are required: the experimental and the calibration particle images. These two types of raw images are recorded in different ways. Figure 2 shows the timing diagram of both the experimental and calibration recordings. The horizontal coordinate is the time axis and the vertical one indicates the snapshot arrangement.  $\Delta t$  denotes the exposure time.  $\Delta t_1$  is the pulse width and  $\Delta t_2$  is the time interval between two neighboring color light pulses.

Figure 2(a) shows the time sequence for the experiment. Three color pulses, denoted as *R*, *G*, and *B*, are triggered to illuminate the flow field in sequence during one exposure time of  $\Delta t$ . Thus, the time intervals should satisfy the relation of

$$3\Delta t_1 + 2\Delta t_2 \leq \Delta t. \quad (1)$$

In the experiment of the present study, a shutter release was used to manually trigger the exposure, which was left open for a long time to cover all three sequential color lights. The exposure ended when the exposure time set in advance was reached. Meanwhile, the computer was programmed to fire three color illuminations through the LCD projector in sequence, starting immediately after the manual trigger. Because the exposure time of the camera is long enough compared with the entire time interval of the color illumination sequence, the three colors can be recorded by the camera in one snapshot. This means that every round of the experiment only takes one raw image, which can also be seen in Figure 1, where the enlarged image shows an individual particle recorded at three instants in one exposure. The triple-exposure recording system in the current experiment is similar to the early PIV techniques of multiple-exposure/single-frame recording systems [20–22]. The main difference in data processing is that the cross-correlation method is applied in TE-CPIV for velocity calculation instead of the auto-correlation used in the early research. The reason is that the color image, including information at three instants, can be separated into three color layers. Each color layer can be considered as one classical PIV recorded image at a certain instant. To reduce the particle image blurs caused by color crosstalk, the color contamination correction will be

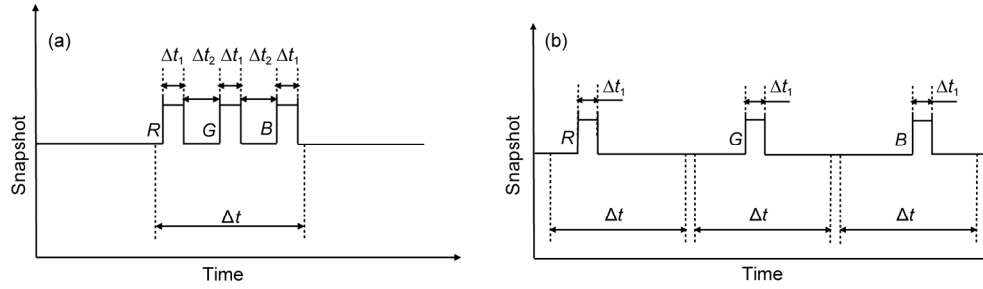


**Figure 2** Pattern of exposure for the triple light pulses of different colors. (a) Timing diagram for experiment; (b) timing diagram for calibration.

performed before the color layer separation.

Figure 2(b) shows the time sequence for the calibration process, which is different from the experimental process. As discussed in Section 2.2, the imaging characteristics of using a color filter array (CFA) and interpolation algorithm to get full resolution of different color layers can cause color contamination. Therefore, the calibration procedure determines the intensity influence of one color illumination on the other two color layers. As shown in the figure, calibration for each color illumination is performed independently. Each single pure color pulse with a pulse width of  $\Delta t_1$  is triggered in one snapshot with an exposure time of  $\Delta t$ . Thus, one single image of the seeded flow field is recorded for each of the three color illuminations. To ensure the calibration environment is exactly the same as that of the experiment condition, the exposure time interval of  $\Delta t$  and pulse width of  $\Delta t_1$  in both experiment and calibration procedures are kept the same. Considering statistical convergence, 5 to 10 calibration images for each color illumination are normally required for contamination calibration. The calibration can be done before or after taking experimental images.

Throughout the process, images are taken in a raw format. This is helpful for color contamination reduction because the uncompressed raw format introduces less contamination, such as white balance, from the recording system. Furthermore, it can provide more abundant intensity levels.

## 2.2 Intensity correction

### 2.2.1 Imaging characteristics

As discussed in Section 2.1, a calibration is conducted to reduce color contamination, which is highly related to the characteristics of the imaging system. In the current work, a common commercial color SLR camera with a CMOS sensor is employed as the recording device, which uses a CFA to produce color components. A filter sensor on every pixel of the CFA panel allows only part of the visible spectrum of light to be recorded [23]. The most commonly used CFA is the Bayer filter array (Figure 3), which has three different kinds of filter sensors designed on the basis of the human visual system. The unit pattern, with a size of  $2 \text{ pixel} \times 2 \text{ pixel}$ , is diagonally arranged with twice as many green sen-

sors as there are red or blue sensors, because human eyes are more sensitive to green color. Because of the discrete arrangement of different color filters in the CFA, a full-resolution color image is obtained with an interpolation process called demosaicking. There are many interpolation algorithms available, such as the bilinear interpolation, pattern recognition interpolation, and the Laplacian color correction method [24]. Unfortunately, all these algorithms can cause color artifacts or noise [23]. Moreover, the interpolation algorithm for an SLR camera is usually unknown to the public and varies with different cameras. Thus, it is impossible to perform an exact reverse engineering approach to recover the original light information on the sensor or totally remove the color contamination.

In addition to the color contamination introduced by demosaicking, the performance of frequency truncation of the color filters also causes color aberration on the image. Ideally speaking, only light with a specific wavelength that is allowed to pass through the filter array can be recorded at the corresponding pixel location. However, in practice, the wavelength range that different filter sensors respond to could have a strong overlap [8]. In other words, light of any wavelength may be detected by all the filter sensors. This effect, coupled with the demosaicking process, results in a decreased signal-to-noise ratio (SNR), which further affects the accuracy of the calculated velocity [25]. Therefore, reduction of color contamination is necessary for color PIV.

### 2.2.2 Contamination reduction

Color contamination happens during both the calibration and experiment imaging processes. The difference is that single-color illumination is recorded in one exposure when operating the calibration, whereas lights of three different colors are recorded together in one exposure during the

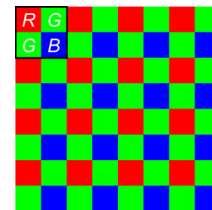


**Figure 3** (Color online) Bayer filter array.

experiment. Therefore, calibration provides the imaging characteristics of each single-color light on the camera. It can be described by a set of calibration functions indicating intensity values of one color illumination on the other two color layers. Because imaging characteristics under different color illuminations are coupled with each other in the experiment, a set of correction equations combines the calibration functions of different color lights to solve the corrected intensity value on each color layer. Thus, the contamination reduction and color layer separation are achieved in three steps:

(1) Acquire the calibration functions for the  $R$ ,  $G$ , and  $B$  illuminations on the basis of the statistical intensity values of one color illumination on the other two color layers.

(2) Estimate the physical particle scattering under each color illumination by solving the correction equations to obtain the corrected intensity values from the raw color layers.

(3) Use the solved intensity values to generate corrected color layers.

In the first step, every calibration image is separated into three color layers corresponding to the three primary colors of  $R$ ,  $G$ , and  $B$ . The intensity level is from 0 to  $2^n-1$ , where  $n$  denotes the bit depth of the recording camera (16 in the present study). To better illustrate the process of obtaining the calibration function, the red color illumination is taken as a typical case for example. Intensity matrices of the three color layers of the calibration image under the red pulse illumination are denoted as  $\mathbf{R}^R$ ,  $\mathbf{G}^R$ , and  $\mathbf{B}^R$ . Here, the variables  $\mathbf{R}$ ,  $\mathbf{G}$ , and  $\mathbf{B}$  represent the three intensity matrices of the different color layers, and the superscript  $R$  means that the light source is a single red color. The pixel position set where intensity is equal to  $v$  in matrix  $\mathbf{R}^R$  is denoted as  $\{(i, j) | \mathbf{R}_{ij}^R = v\}$ .  $v$  is the intensity range within a closed interval of  $[0, 2^n-1]$ , and  $(i, j)$  is the row and column indexes. If the resolution of the image is  $M$  pixel  $\times$   $N$  pixel, the range of  $i$  and  $j$  are  $1 \leq i \leq M$  and  $1 \leq j \leq N$ . It should be noted that every separate color layer has the same resolution of  $M \times N$ . Here, it is assumed that the intensity of every pixel of  $\mathbf{R}^R$  is the physical intensity of particle scattering under the red illumination. For all  $(i, j) \in \{(i, j) | \mathbf{R}_{ij}^R = v\}$ , the intensity of particle scattering is also recorded on the  $G$  layer because of color contamination, and the intensity values at the corresponding location set of  $(i, j)$  on the  $G$  layer are not the same for the sensitivity difference of the different color filter sensors. The average of these values is taken as the contribution of the  $R$  pulse illumination on the  $G$  layer (namely, matrix  $\mathbf{G}^R$ ) when the intensity of the  $R$  illumination is  $v$ . Therefore, a relation between the intensity on  $\mathbf{G}^R$  and that on  $\mathbf{R}^R$  is obtained. The contribution of each color illumination to the other different color layers can be acquired in the same way. In summary, the recorded intensity of all the color illuminations on the different color layers follows functions of

$$\begin{cases} f_R^R(v_R) = \frac{1}{n_{v_R}} \sum_{i,j} \mathbf{R}_{ij}^R = v_R, \\ f_G^R(v_R) = \frac{1}{n_{v_R}} \sum_{i,j} \mathbf{G}_{ij}^R, & \{(i, j) | \mathbf{R}_{ij}^R = v_R\}, \\ f_B^R(v_R) = \frac{1}{n_{v_R}} \sum_{i,j} \mathbf{B}_{ij}^R, \end{cases} \quad (2)$$

$$\begin{cases} f_R^G(v_G) = \frac{1}{n_{v_G}} \sum_{i,j} \mathbf{R}_{ij}^G, \\ f_G^G(v_G) = \frac{1}{n_{v_G}} \sum_{i,j} \mathbf{G}_{ij}^G = v_G, & \{(i, j) | \mathbf{G}_{ij}^G = v_G\}, \\ f_B^G(v_G) = \frac{1}{n_{v_G}} \sum_{i,j} \mathbf{B}_{ij}^G, \end{cases} \quad (3)$$

$$\begin{cases} f_R^B(v_B) = \frac{1}{n_{v_B}} \sum_{i,j} \mathbf{R}_{ij}^B, \\ f_G^B(v_B) = \frac{1}{n_{v_B}} \sum_{i,j} \mathbf{G}_{ij}^B, & \{(i, j) | \mathbf{B}_{ij}^B = v_B\}, \\ f_B^B(v_B) = \frac{1}{n_{v_B}} \sum_{i,j} \mathbf{B}_{ij}^B = v_B, \end{cases} \quad (4)$$

where  $f_G^R(v_R)$  is the calibration function representing the intensity contamination of the  $R$  pulse illumination on  $\mathbf{G}^R$  when the recorded intensity on  $\mathbf{R}^R$  is  $v_R$ . The superscript  $R$  and subscript  $G$  of  $f_G^R$  represent the single red pulse illumination and the intensity matrix of the green layer, respectively.  $v_R$  denotes the intensity of  $v$  on the  $R$  layer.  $n_{v_R}$  is the number of pixels in the set  $\{(i, j) | \mathbf{R}_{ij}^R = v_R\}$ . This nomenclature is the same for all symbols of different colors.

The expression of the calibration function can be acquired by a curve fitting of the intensity on the color layers versus the intensity of the illumination. From eq. (2), it can be seen that  $f_R^R(v_R)$  should be a linear function with a slope of 1. Second-order polynomial fitting is used to fit the calibration functions of the red illumination on the  $G$  and  $B$  layers. Thus, as an example, the calibration function of the  $G$  layer under red illumination has the form of

$$f_G^R(v_R) = av_R^2 + bv_R + c, \quad (5)$$

where  $a$ ,  $b$ , and  $c$  are the fitting parameters. In the same way, we can obtain the other calibration functions. It should be noted that similar ideas for color contamination procedures were also proposed by other researchers without specific calibration in a raw format [5,6,13,18]. Generally, a first-order linear function was used in previous studies. However, as will be shown in Section 3, a first-order linear function is not sufficient to represent the calibration func-

tion when the calibration is operated on the raw format images. Therefore, a parabolic function as in eq. (5) is applied.

The second step is to construct a correction equation for the experimental image. The correction equation is formed by combining the calibration functions of the three color illuminations because contaminations of the three different color illuminations are coupled together during the experiment. In other words, nine calibration functions should generate three intensity correction equations on every pixel. Therefore, for a resolution of  $M$  pixel  $\times$   $N$  pixel, there will be  $3 \times M \times N$  correction equations over all pixels. The correction equations have the form of

$$\begin{cases} R_{\text{read}} = f_R^R(R_{\text{cor}}) + f_R^G(G_{\text{cor}}) + f_R^B(B_{\text{cor}}), \\ G_{\text{read}} = f_G^R(R_{\text{cor}}) + f_G^G(G_{\text{cor}}) + f_G^B(B_{\text{cor}}), \\ B_{\text{read}} = f_B^R(R_{\text{cor}}) + f_B^G(G_{\text{cor}}) + f_B^B(B_{\text{cor}}), \end{cases} \quad (6)$$

where,  $R_{\text{read}}$ ,  $G_{\text{read}}$ , and  $B_{\text{read}}$  represent the raw intensity values on the  $R$ ,  $G$ , and  $B$  layers, respectively, of the experimental image. These values are already known and can be directly read from the recorded image.  $R_{\text{cor}}$ ,  $G_{\text{cor}}$ , and  $B_{\text{cor}}$  represent the corresponding corrected intensity values. These values are unknown and can be obtained by solving the correction equations for every pixel.

Eq. (6) is in a ternary quadratic form and is solved using the solve function in MATLAB in the present work. More than one solution of eq. (6) exists. For every unknown, there are two real solutions and six complex solutions (three sets of conjugated solutions). It is easy to determine the true root that satisfies our requirement because only one real solution satisfies the intensity range of 0 to  $2^n - 1$ . Unfortunately, the relation between the rest of the solutions and the imaging system is currently unclear. Note that the light intensity is usually adjusted to avoid intensity saturation when taking images. Correcting the intensity value by solving the equations could happen to result in a negative value when the raw intensity is close to 0 because of different response characteristics of the CMOS sensors. A negative value will be reassigned as 0. Because this phenomenon exists only on pixels with very small raw intensity values, it has little influence on the further cross correlation result of determining velocity. As a result, we can obtain the corrected intensity matrix for each color layer. Finally, the corrected intensity is used to generate three new color layers. The contamination reduction and color layer separation are all performed in MATLAB.

### 2.3 Pressure reconstruction method

After a standard PIV correlation process to obtain two velocity fields based on the three corrected color layers, pressure can be reconstructed. Pressure is related to velocity on the basis of the N-S equations for incompressible flows as [1]

$$\nabla p = -\rho \frac{D\mathbf{u}}{Dt} + \mu \nabla^2 \mathbf{u}, \quad (7)$$

where  $\nabla p$  is the pressure gradient,  $\rho$  is the fluid density,  $\mathbf{u}$  is the velocity vector,  $D\mathbf{u}/Dt$  denotes the material acceleration, and  $\mu \nabla^2 \mathbf{u}$  is the viscous term. Because the viscous term is usually at least two orders of magnitude smaller than the material acceleration term, it is neglected in the following discussion [26–28].

Eulerian and Lagrangian approaches have been developed to calculate material acceleration [4,29]. The latter one is applied in the present work because some researchers found that the Lagrangian approach seems to be less sensitive to measurement noise [30,31]. The material acceleration could be expressed in Lagrangian perspective as

$$\frac{D\mathbf{u}}{Dt} = \frac{d\mathbf{u}_p(t)}{dt} = \frac{d\mathbf{u}(\mathbf{x}_p(t), t)}{dt}, \quad (8)$$

where  $\mathbf{x}_p(t)$  and  $\mathbf{u}_p(t)$  are the position and velocity, respectively, of the traced virtual particle at time  $t$ . Eq. (8) can be discretized in a central difference scheme as

$$\left. \frac{D\mathbf{u}}{Dt} \right|_{\mathbf{x}+\mathbf{u}_a\Delta t/2, t+\Delta t/2} = \frac{\mathbf{u}_2(\mathbf{x}+\mathbf{u}_a\Delta t, t+\Delta t) - \mathbf{u}_1(\mathbf{x}, t)}{\Delta t}, \quad (9)$$

where  $\Delta t$  is the temporal step;  $\mathbf{u}_a$  denotes the averaged Lagrangian velocity of the traced virtual particle between time  $t$  and  $t+\Delta t$ , whose position is  $\mathbf{x}$  at time  $t$  and  $\mathbf{x}+\mathbf{u}_a\Delta t$  at time  $t+\Delta t$ ; and  $\mathbf{u}_1$  and  $\mathbf{u}_2$  are the velocity of the traced particle at time  $t$  and  $t+\Delta t$ , respectively.  $\mathbf{u}_a$  is calculated as

$$\mathbf{u}_a(\mathbf{x}+\mathbf{u}_a\Delta t/2, t+\Delta t/2) = \frac{\mathbf{u}_1(\mathbf{x}, t) + \mathbf{u}_2(\mathbf{x}+\mathbf{u}_a\Delta t, t+\Delta t)}{2}. \quad (10)$$

An iterative approach is employed to obtain  $\mathbf{u}_a$  [4]. In the first iteration step,  $\mathbf{u}_1$  is used as  $\mathbf{u}_a$  so that we can obtain  $\mathbf{u}_2$  at the position of  $\mathbf{x}+\mathbf{u}_1\Delta t$ . The iteration stops when the ratio  $\left| \frac{\mathbf{u}_{a,\text{old}} - \mathbf{u}_{a,\text{new}}}{\mathbf{u}_{a,\text{new}}} \right|$  is less than 0.001.  $\mathbf{u}_{a,\text{new}}$  and  $\mathbf{u}_{a,\text{old}}$  are the latest calculated and the last calculated  $\mathbf{u}_a$  in two neighboring time steps. The overbar “—” and “|·|” denote the mean value and the absolute value, respectively.

After the pressure gradient is obtained, an irrotation correction is performed following the work of Wang et al. [32] to improve the accuracy of pressure reconstruction. This correction is based on the knowledge that  $\nabla p$  should be irrotational. However, the calculated pressure gradient field from the experiment normally does not satisfy the condition of irrotation because of measurement errors. Denoting the curl operator of the calculated pressure gradient field as  $\mathbf{A}$ ,

we have

$$\mathbf{A}\mathbf{G}=0. \quad (11)$$

where  $\mathbf{G}$  denotes the irrotational field that would be determined by solving eq. (11) with the function of null in MATLAB. Thus, a set of orthogonal basis could be obtained that can span the irrotational space of  $\mathbf{G}$ . With the original noisy pressure gradient projected onto this set of orthogonal basis, the corrected pressure gradient can be acquired to satisfy the irrotation condition.

Then, pressure is determined by a spatial integration along orthogonal integral paths, expressed as

$$p(s_{\text{tar}}) = p(s_{\text{ref}}) + \int_{s_{\text{ref}}}^{s_{\text{tar}}} \nabla p \cdot ds, \quad (12)$$

where  $s$  denotes the integration variable of the particle location, and  $p(s_{\text{ref}})$  and  $p(s_{\text{tar}})$  are the pressure values at the reference location and target location, respectively. A second-order central difference scheme is used during the integration process. Because pressure is calculated by direct integration on the pressure gradient field, no Neumann boundary condition is required. Thus, a Dirichlet boundary condition of pressure at a reference location,  $p(s_{\text{ref}})$ , is sufficient. It should be noted that the reconstructed pressure is relative to the pressure at the reference location. More details of the pressure reconstruction and the irrotation correction technique can be found in Wang et al. [32].

### 3 Experimental validation

Two experiments were conducted to validate the capability of the TE-CPIV technique to determine velocity field and the coupled pressure field, using a rotating solid body flow and a cylinder wake flow. A projector for producing illumination and a digital color SLR camera with a CMOS sensor were used in the experiments; both devices are common and easily procured. Different brands of cameras were applied to the two flow cases to prove the robustness of the contamination correction algorithm on different imaging systems.

#### 3.1 Rotating solid body flow

A rotating solid body flow was investigated to assess the TE-CPIV method, which is a reliable test case for assessment [4,16]. Figure 4 shows the arrangement of the experimental setup. The flow was simulated with a rotating rigid plate driven by a motor at a speed of approximately  $\omega = 0.26$  rad/s. The plate was painted with matte paint. Similar to seeding tracers in a water flow, hollow glass beads with a mean diameter of  $5 \mu\text{m}$  were uniformly seeded and stuck on the plate surface. To reduce the cost and simplify the experimental platform, a BENQ W1100 LCD projector with brightness of 2000 lumens was used as the light source. A

computer was utilized to control the LCD projector to produce different color illuminations. Three different color lights of  $R$ ,  $G$ , and  $B$  were projected in a time sequence. The pulse width was  $\Delta t_1 = 0.04$  s. Between the temporal interval of  $\Delta t_2 = 0.1$  s every two color pulses, black background light was projected. The rotating plate was directly illuminated by the projection light. A Canon EOS400D digital camera was used as the image recorder with a measurement resolution of  $600 \text{ pixel} \times 600 \text{ pixel}$  for a domain of  $67.32 \text{ mm} \times 67.32 \text{ mm}$ . The camera was manually controlled to record particle images with the three color illuminations in one exposure time of  $\Delta t$ . To satisfy the relation of eq. (1),  $\Delta t$  was set to 0.6 s. The  $f$  number of the aperture was set to 8 and the photo sensitivity (by International Standards Organization, ISO) was 800. The images were taken in the raw format whose bit depth for a single color was 16, which means the intensity of a single color can vary from 0 to 65535 ( $2^{16} - 1$ ).

#### 3.1.1 Performance of color contamination reduction

Calibration was operated for each color of light. The pulse width and exposure time were kept the same as the settings in the experiment. In calibration, the flow field was recorded under only one single-color illumination during each exposure, which resulted in three raw particle images under three different color illuminations. A statistical analysis was performed following eqs. (2)–(5) to obtain the calibration functions of the recording system. Figure 5 shows the influence of every single-color illumination on the other different color layers. The horizontal axis represents the intensity of the color illumination on the corresponding color layer of the camera, whereas the vertical axis represents the contaminated intensity on the other color layers. Scattered points are the averaged contamination intensity. The curved line is the second-order fitting curve of the scattered points, and its expression is given as the calibration function (eq. (5)).

As can be seen from the figure, a first-order linear function is not sufficient to depict the relation between the contaminated intensity and the color illumination intensity. That is why a second-order fitting polynomial is used. The

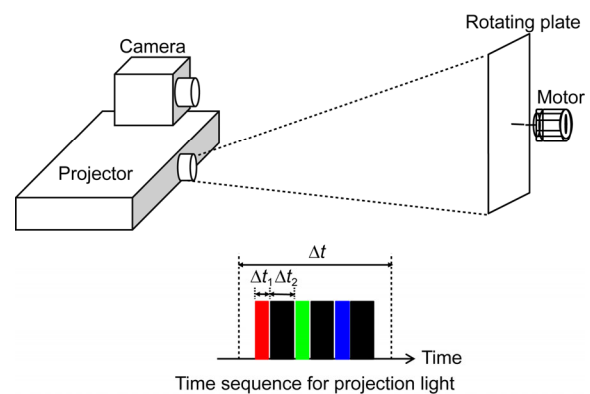
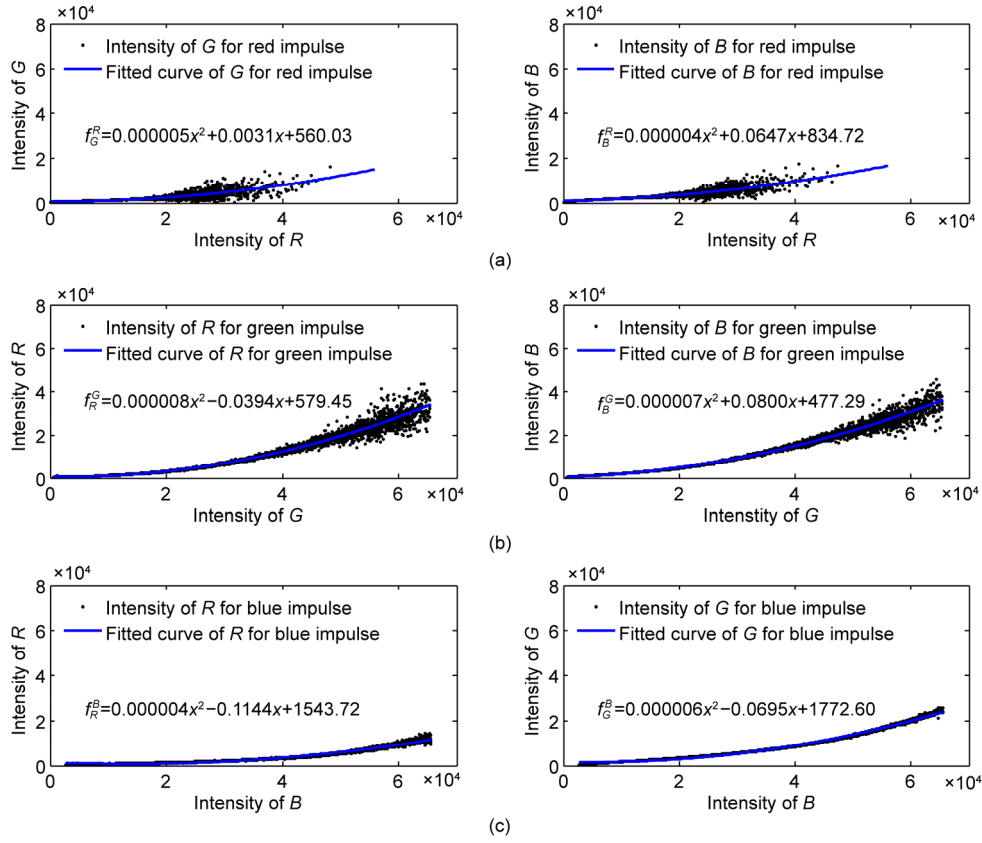


Figure 4 (Color online) Setup of the solid body rotation experiment.



**Figure 5** (Color online) Calibration function for different color light sources. (a) Calibration function under  $R$  illumination; (b) calibration function under  $G$  illumination; (c) calibration function under  $B$  illumination.

calibration function for the color illumination on the image layer of the same color is not given because it should be a linear function with a slope of 1 on the basis of the definition in Section 2.2.2. It seems that the camera is not sensitive to red light, because the intensity values on the red layer under the red illumination (the horizontal coordinate of Figure 5(a)) is mainly distributed below  $4 \times 10^4$ . Under the green (Figure 5(b)) and blue (Figure 5(c)) illuminations, the intensity values on the  $G$  layer and  $B$  layer have a wider range of distribution, up to  $6.5 \times 10^4$ . The contamination of the green illumination on the other two color layers (the vertical coordinate of Figure 5(b)) is the strongest. Therefore, the contaminations of different color lights on different color layers are not the same. Furthermore, the scattered points have some level of deviation from the fitting curves. This is partly because of the different response sensitivity of different filtering sensors. Another primary reason is the use of a simplified second-order polynomial fitting to approximate the contaminated intensity, whereas the real contamination results from comprehensive reasons such as the illumination device, light-scattering property of the particles, and the optical receiving property of a camera [13]. Generally speaking, the less deviated the contamination of color light on a color layer, the more accurate the fitting model. Thus, estimation of the contaminated intensity for the blue

illumination is assumed to be the most accurate one in this test case.

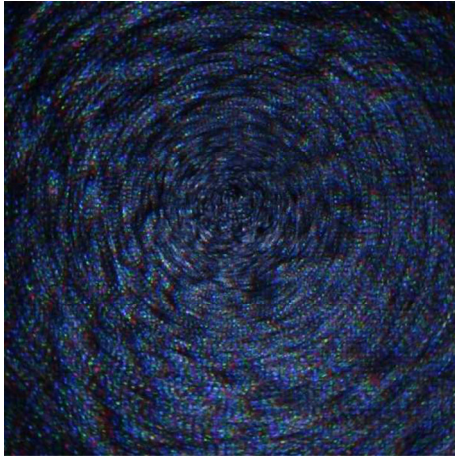
These calibration functions in Figure 5 represent contamination characteristics for every single-color illumination. For the experimental image, contaminations of different color illuminations are coupled together. Thus, calibration functions should be combined to decouple and reduce color contamination. Substituting the calibration functions into eq. (6), we can obtain a set of correction equations at each pixel:

$$\begin{cases} R_{\text{read}} = R_{\text{cor}} + 0.000008G_{\text{cor}}^2 - 0.0394G_{\text{cor}} \\ \quad + 0.000004B_{\text{cor}}^2 - 0.1144B_{\text{cor}} + 2123.17, \\ G_{\text{read}} = 0.000005R_{\text{cor}}^2 + 0.0031R_{\text{cor}} + G_{\text{cor}} \\ \quad + 0.000006B_{\text{cor}}^2 - 0.0695B_{\text{cor}} + 2332.63, \\ B_{\text{read}} = 0.000004R_{\text{cor}}^2 + 0.0647R_{\text{cor}} + 0.000007G_{\text{cor}}^2 \\ \quad + 0.0800G_{\text{cor}} + B_{\text{cor}} + 1312.01. \end{cases} \quad (13)$$

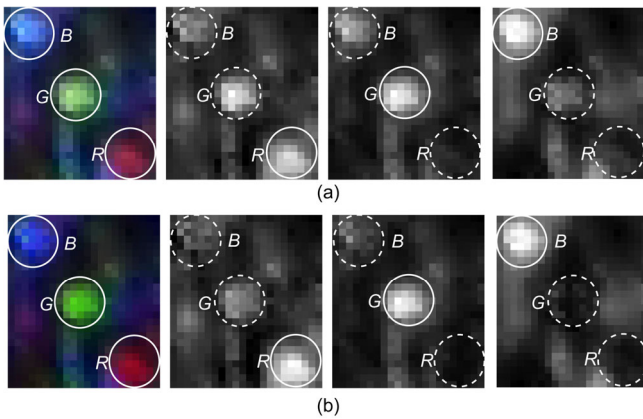
Here,  $R_{\text{read}}$ ,  $G_{\text{read}}$  and  $B_{\text{read}}$  denote the intensity that can be read directly from the separated color layers of the raw experimental image.  $R_{\text{cor}}$ ,  $G_{\text{cor}}$ , and  $B_{\text{cor}}$  are the corrected intensity values solved from the equations as the corresponding reasonable intensity to generate new color layers.

Figure 6 is an example of the raw experimental image.

The plate was rotating clockwise. Particles under different color illuminations were recorded at different instants in one exposure. In the current work, the image quality on the upper side was not as good as that on the lower side because of the viewing angle. The experimental image was then separated into three raw color layers, resulting in  $R_{\text{read}}$ ,  $G_{\text{read}}$ , and  $B_{\text{read}}$  on every pixel.  $R_{\text{cor}}$ ,  $G_{\text{cor}}$ , and  $B_{\text{cor}}$  were obtained by solving eq. (13) for generating new color layers, which were used to deduce velocity. To show the effect of the contamination correction, enlarged particle images as well as separated color layers are shown in Figure 7. An individual particle (circled in the figure) at three different instants (marked by  $R$ ,  $G$ , and  $B$ ) was captured by the camera. Figure 7(a) shows the separated color layers of the raw image, and Figure 7(b) shows the new color layers after contamination correction. The dashed line circles the contaminated ghost particle image that needs to be corrected. It can be seen in Figure 7(a) that each of the original separated color



**Figure 6** (Color online) Experimental color image of the rotating plate.



**Figure 7** (Color online) Images of an individual particle at different instants before and after the intensity correction. (a) Separated color layers of the raw image; (b) new color layers after contamination correction (the first column shows the color particle images under three color illuminations. The second, third, and fourth column are particle images of the  $R$  layer,  $G$  layer, and  $B$  layer, respectively).

layers is influenced by all color illuminations. Therefore, the image of the particle under different color illuminations cannot be well-separated. After intensity correction, the influence of the color light on other different color layers is apparently reduced although not totally removed.

### 3.1.2 Velocity calculation and error analysis

After the contamination correction and image separation, velocity was calculated using the classical PIV procedure of cross-correlation. With three corrected color layers, two velocity fields could be obtained. One velocity was from the  $R$  and  $G$  color layers, and the other was from the  $G$  and  $B$  color layers. Multi-grid iteration with image deformation [33] was applied in this process with the initial window size of  $128 \text{ pixel} \times 128 \text{ pixel}$  and the final window size of  $32 \text{ pixel} \times 32 \text{ pixel}$ . The overlap was chosen as 50%. A least-square Gauss fitting in a  $3 \times 3$  window was applied to determine the sub-pixel correlation peak. Outliers in the velocity field were removed through an average smoothing with a kernel of  $3 \times 3$  nodes [25]. Because the rotation flow was steady, velocity fields were averaged [34] with ten instants to reduce the influence of the fluctuated motor driving speed. Theoretical velocity fields were calculated for comparison.

The rotation center of the theoretical velocity must be carefully determined to avoid raising a large bias error [35] similar to the bias error of finding the peak in the correlation. All radius vectors associated with the local velocity vectors should pass the rotation center in a rigid body rotation. For a point whose coordinate is denoted as  $(x_0, y_0)$ , the equation of the line along the radius vector at this point can be expressed as

$$y - y_0 = -\frac{u_0}{v_0}(x - x_0), \quad (14)$$

where  $u_0$  and  $v_0$  denote the magnitude of the velocity components at the point of  $(x_0, y_0)$ . Therefore, the question to determine the rotation center of  $(x_c, y_c)$  becomes a matrix equation of

$$\begin{pmatrix} \frac{u_1}{v_1} & 1 \\ \vdots & \vdots \\ \frac{u_n}{v_n} & 1 \end{pmatrix} \begin{pmatrix} x_c \\ y_c \end{pmatrix} = \begin{pmatrix} y_1 + \frac{u_1}{v_1} x_1 \\ \vdots \\ y_n + \frac{u_n}{v_n} x_n \end{pmatrix}, \quad (15)$$

where  $n$  is the index of the grid nodes. A least-square solution can be obtained, which makes the summation of the distance between the rotation center and the radius vectors the smallest. After the rotation center is obtained, the theoretical velocity fields can be calculated.

Besides the bias error, random error always exists in the measurement. Therefore, both the bias and random errors are investigated. The bias error and random error are de-

finned following McKenna et al. [36] and Huang et al. [37] as

$$\varepsilon_{\text{bias}} = \overline{X}_e - X_t, \quad (16)$$

$$\varepsilon_{\text{random}} = \sqrt{\frac{1}{N} \sum_{i=1}^N (X_i - \overline{X}_e)^2}, \quad (17)$$

where  $X_i$  are the measurement samples that should have the same theoretical displacements.  $\overline{X}_e$  is the spatial mean of  $X_i$ , whose number is  $N$ .  $X_t$  is the theoretical displacement. For the rotation flow, the horizontal displacement should be constant along each horizontal row. Therefore, the average of the horizontal displacements is taken to compute  $\overline{X}_e$  in the horizontal direction along each row. Similarly, the average of the vertical displacements along each column is taken to compute  $\overline{Y}_e$  in the vertical direction [34]. Figure 8 shows the bias errors and random errors for both the  $R, G$  layers and  $G, B$  layers. The mean magnitude of the bias errors in both directions in Figure 8(a) and (b) is approximately 0.33 pixel, which is somewhat larger than the general PIV measurement uncertainty of 0.1 pixel, but is acceptable. The mean values of the random error magnitude in the horizontal and vertical directions (Figure 8(c) and (d)) are approximately 0.07 pixel, which is at the same level as the classical PIV result [36,38]. As a result, the displacement errors are regarded as at a similar level to the classical PIV, and are acceptable.

The total velocity magnitude is defined as  $V = \sqrt{u^2 + v^2}$ . Figure 9 shows the velocity fields determined by the  $R$  and  $G$  color layers and the  $G$  and  $B$  color layers, as well as the theoretical velocity field. Coordinates are non-dimensionalized by the maximum rotation radius of  $r_{\text{max}}$ . Velocity fields are non-dimensionalized by a reference velocity of  $V_{\text{ref}} = r_{\text{max}} \omega$ , where  $\omega$  is the rotation angular velocity controlled by the driving motor. To have the rotation center at the centroid of the figure, the boundary of the figure is cropped slightly. A definition of relative error for velocity is given as

$$\varepsilon_v = \frac{|V_e - V_t|}{V_{\text{ref}}}, \quad (18)$$

where  $V_e$  and  $V_t$  are the measured experimental velocity and the theoretical velocity at every node, respectively.  $\varepsilon_v$  represents the mean error value over all velocity fields.  $\varepsilon_v$  for each of the calculated velocity fields are 3.9% and 3.3%. Velocity distribution on the upper side is not as good as that on the lower side compared to the theoretical velocity. This is mainly because of the raw image quality in different regions, which can also be seen in the raw image of the flow (Figure 6). The correlation coefficient between the velocity fields in Figure 9(a) and that in Figure 9(c) is 0.9928, whereas the correlation coefficient between the velocity fields in Figure 9(b) and that in Figure 9(c) is 0.9925. Therefore, TE-CPIV can determine velocity with high accuracy.

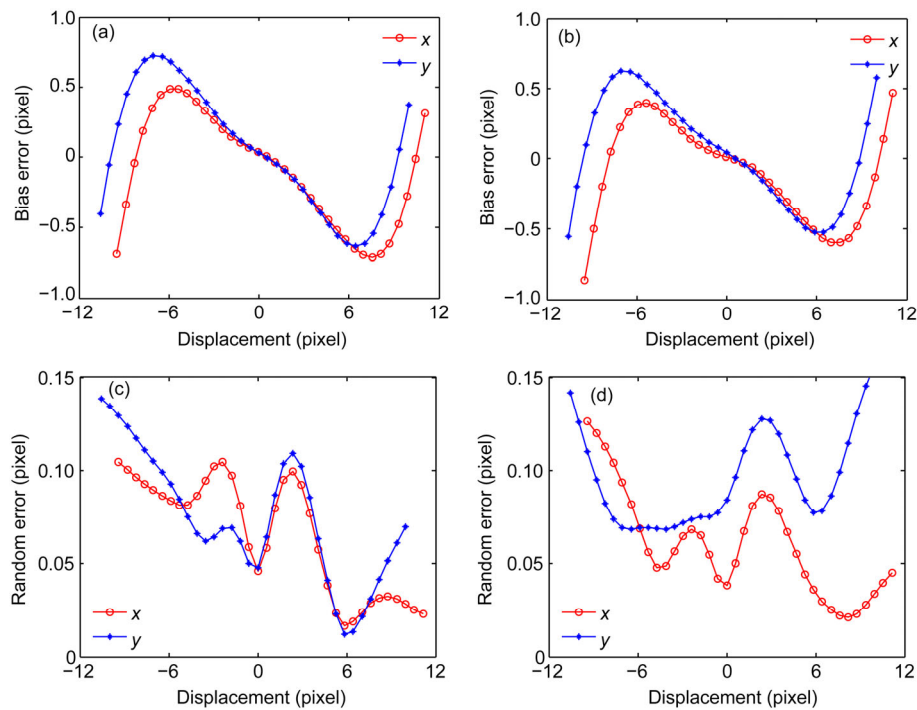


**Figure 8** (Color online) Bias errors and random errors for both the  $R, G$  layer and  $G, B$  layer. (a) Bias error for the  $R, G$  layer; (b) bias error for the  $G, B$  layer; (c) random error for the  $R, G$  layer; (d) random error for the  $G, B$  layer.

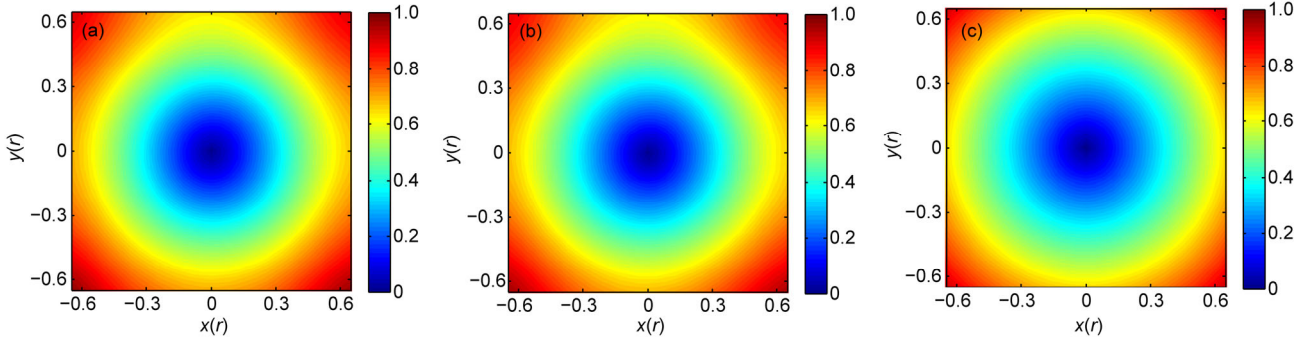


**Figure 9** (Color online) Velocity field comparison. (a) Experimental velocity for the  $R, G$  layer; (b) experimental velocity for the  $G, B$  layer; (c) theoretical velocity. Velocity is non-dimensionalized by  $V_{\text{ref}}=r_{\text{max}}\omega$ , where  $r_{\text{max}}$  is the maximum rotation radius and  $\omega$  is the rotation angular velocity.

### 3.1.3 Pressure calculation and error analysis

Material acceleration is obtained in the Lagrangian coordinate as described in Section 2.3. Then, pressure is integrated through an orthogonal path integration method on the basis of the calculated pressure gradient field (mainly material acceleration) [32]. During integration for pressure, a reference location is selected at the center of the rotation plate, and the corresponding pressure is assigned as 0. This is the Dirichlet boundary condition, which is sufficient for pressure integration on the known pressure gradient field. The final experimental pressure and the theoretical pressure are shown in Figure 10. Coordinates are non-dimensionalized by  $r_{\text{max}}$ , and pressure is non-dimensionalized by a reference pressure of  $p_{\text{ref}} = \rho r_{\text{max}}^2 \omega^2 / 2$ . Clearly, pressure calculated from the TE-CPIV determined velocity (Figure 10(a)) is close to the theoretical pressure distribution (Figure 10(b)). However, the concentricity is not as good on the upper side of the field because of the measurement error in the velocity fields (Figure 9), whereas the lower part has better concentricity and accuracy. A relative error of pressure is defined as  $\varepsilon_p = |p_e - p_t| / p_{\text{ref}}$ , where  $\varepsilon_p$  is the calculated experimental pressure and  $p_t$  is the theoretical pressure. Then,  $\varepsilon_p$  was calculated to be 4.44%. The correlation coefficient

between pressure values in Figure 10(a) and (b) is approximately 0.9751. This indicates that pressure reconstructed from the TE-CPIV determined velocity also has an acceptable accuracy.

### 3.2 Cylinder wake flow

The TE-CPIV method was also applied in a cylinder wake flow experiment to assess its performance. The experiment was conducted in the water channel in the Beijing University of Aeronautics and Astronautics, and the experimental setup is shown in Figure 11(a). The water channel has an experiment section of 600 mm × 700 mm × 3000 mm. A cylinder with a diameter of  $d = 20$  mm was fixed in the channel. The free stream velocity was 16.7 mm/s and the Reynolds number based on the cylinder diameter was 371. Tracer particles seeded into the channel were hollow glass beads with a mean diameter of 5  $\mu\text{m}$ . The same LCD projector as in the experiment of solid body rotation flow was used to produce a sequence of color illuminations ( $R, G$ , and  $B$ ). Two cylindrical lenses were employed to modulate the volumetric light source into a planar light sheet (Figure 11(b)). The focal lengths of the two lenses were 200 and 50 mm. Volumetric illumination from the projector cannot be modulated into a perfect planar light sheet with only two

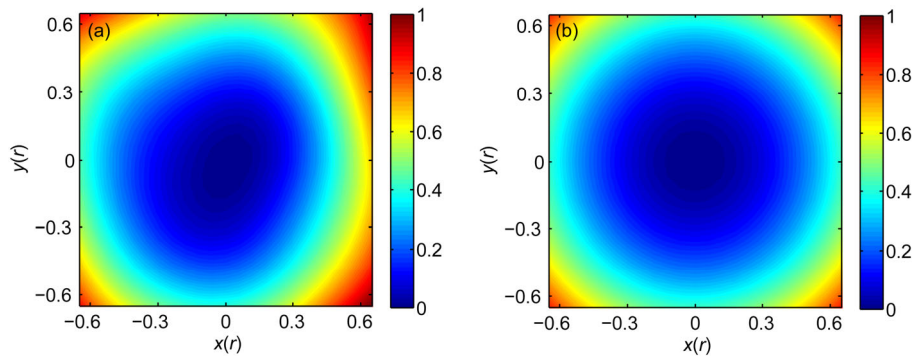


**Figure 10** (Color online) Pressure field comparison. (a) Experimental pressure; (b) theoretical pressure. Pressure is non-dimensionalized by  $p_{\text{ref}} = \rho r_{\text{max}}^2 \omega^2 / 2$ , where  $r_{\text{max}}$  is the maximum rotation radius and  $\omega$  is the rotation angular velocity.

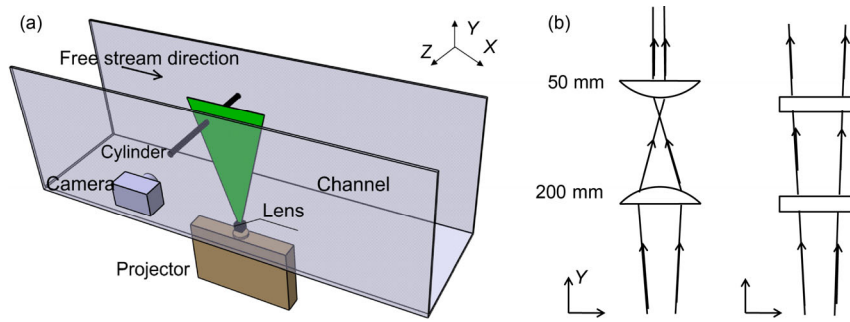


**Figure 11** (Color online) Setup of the cylinder wake flow experiment. (a) Arrangement of the setup; (b) optical path diagram.

lenses. Therefore, black light-proof paper was used to cover the side of the light sheet to generate a thin light sheet of less than 2 mm thickness. Because light from the projector is already divergent, there is no need to use an additional lens to generate divergent light along the free stream direction. To test the robustness of TE-CPIV on different cameras, a NIKON D3100 digital camera was utilized as the color image recorder in this case. The measurement domain was  $64.2 \text{ mm} \times 47.5 \text{ mm}$  ( $X \times Y$ ) and the resolution for this domain was  $1287 \text{ pixel} \times 951 \text{ pixel}$ . Thus the magnification factor was  $0.05 \text{ mm/pixel}$ . The pulse width for every color light was  $\Delta t_1 = 0.03 \text{ s}$ . The temporal interval between neighboring color light pluses in this experiment was  $\Delta t_2 = 0.05 \text{ s}$ . The exposure time for the camera was  $\Delta t = 0.3 \text{ s}$  so that the three temporal intervals satisfied eq. (1).

Meanwhile, the classical planar PIV method was also operated to measure the flow as a comparison. The arrangement of the classical PIV measurement setup was similar to the TE-CPIV measurement, except that illumination was produced by a 5-W continuous semiconductor laser of 532 nm wavelength, and the image recorder was a high-speed CCD camera (ICL-B0620, IMPERX Co. Ltd.). The camera had a resolution of  $640 \text{ pixel} \times 480 \text{ pixel}$  with a Nikon 45-mm lens. The measurement domain was  $73.1 \text{ mm} \times 54.8 \text{ mm}$ , which was somewhat larger than the measurement domain in the TE-CPIV experiment. The magnification factor was  $0.11 \text{ mm/pixel}$ . The exposure time was 5 ms, and the sampling frequency of the classical PIV was 50 Hz. Color calibration and intensity correction were performed to generate separate color layers with corrected intensity as described in Section 3.1.

The same PIV processing for velocity as in the solid body rotation experiment was applied to the corrected color layers. As a result, the velocity vectors had a resolution of 1.6 mm and the vector space was 0.8 mm in each direction. A robust all-in-one method [39] was used to improve the velocity accuracy. A divergence-free smoothing algorithm [40] was further performed to improve the velocity field for satisfying the zero-divergence condition of incompressible flow. For the classical PIV experiment, the same cross-correlation method was applied with the initial interrogation window of  $64 \text{ pixel} \times 64 \text{ pixel}$  and the final window

size of  $16 \text{ pixel} \times 16 \text{ pixel}$ . Overlap was still chosen as 50%. Therefore, velocity vectors in this case had a resolution of 1.8 mm, and the vector space was 0.9 mm in both directions, which was similar to that in the TE-CPIV. For a future comparison, the post-processing procedures on the velocity field in the classical PIV were maintained the same as the TE-CPIV. To assess the performance of TE-CPIV, velocity fields of both classical PIV and TE-CPIV in the same region of the measurement domain were extracted. Velocity from TE-CPIV was interpolated onto the same grid of the classical PIV field.

Although the two different experiments measured the same flow, they were performed separately, which means that the velocity fields in the two experiments could not be obtained simultaneously. Fortunately, the cylinder flow is a quasi-periodic flow. Thus, velocity fields at the same phase in the two experiments can be matched for comparison through a phase-matching method [41]. The global periodicity of the cylinder flow was investigated via the proper orthogonal decomposition (POD) on velocity from classical PIV [42]. A statistical investigation to the time coefficient of the POD modes from 5000 velocity fields showed that the cylinder wake flow had a good periodicity with a vortex shedding period of approximately 5.88 s. To match the TE-CPIV velocity phase with the classical one, velocity from TE-CPIV in the same region with all the classical PIV velocity fields are compared during a period through a cross correlation. Velocity fields with the highest correlation peak were assumed to be in a similar phase. Because the sample frequency of the classical PIV was 50 Hz and the vortex shedding period was 5.88 s, approximately 294 images were recorded for every period. Uncertainty of the phase matching should be under  $1.23^\circ$ .

Figure 12 shows the velocity fields from the two PIV experiments at similar phases. The coordinate was non-dimensionalized by the cylinder diameter. It is obvious that TE-CPIV can capture the flow structure as well as the classical PIV. The correlation coefficient between the velocity field from TE-CPIV and that from classical PIV is 0.9628. This indicates that TE-CPIV can realize the velocity measurement at a similar precision to the classical PIV.

The pressure gradient field and pressure field were then

calculated using the same method as in the experiment of solid body rotation flow. Figure 13 shows the reconstructed pressure fields from the velocity fields in the two experiments. The structure of the vortex is well detected by both TE-CPIV and classical PIV. The correlation coefficient between these two pressure results is 0.9407. Considering that the two pressure fields are not perfectly phase-matched, the correlation coefficient is acceptable. Therefore, all the comparisons suggest that pressure could be reconstructed through the TE-CPIV method with lower cost and more accessible devices than the classical PIV.

It needs to be reminded for a more thorough understanding of the developed technique. The main idea of the TE-CPIV is to associate the color information of a camera with the temporal information of a flow and connect the color PIV technique with pressure reconstruction. The application of the new technique is not limited to the examples in this article, which represents a simple setup with a projector and an SLR camera. Because of the simplest configuration of the devices used in the present tests, several limitations exist. One of the main limitations is the sample frequency, which is determined by both the refresh frequency of the projector and the recording repetition frequency of the SLR camera. As a result, the current devices are not applicable to high-speed flow measurement, because they are not able to generate a very small time interval among color lights via projector for high-speed flows. Better devices, such as pulsed LED as a light source and a high-

speed camera for the image recording, could make this application feasible for high-speed flows. Another main limitation is the synchronization between the color illuminations and the camera. As described previously in Section 2.1, the synchronization in the tests was performed manually. The following examples show other alternative choices for light illumination and imaging devices, which makes this technique more applicable. To break through the refresh frequency limitation of the projector, a rotating polygonal mirror [9,16] with different filters on different surfaces could be used. To improve the illumination energy, light-emitting diodes [16] and laser light [43] are alternative choices. To obtain time-resolved velocity and pressure, a digital color camera with higher repetitive frequency [44] or video camera [10,13] could be used as the image recorder. To reduce the color contamination of the recording camera, a 3-CCD color camera [5,12] without intensity interpolation for full-resolution color layer can be considered. The simultaneous control of the illumination and camera exposure could also be improved, because many digital color cameras can be triggered by a computer transistor-transistor logic (TTL) signal [45].

## 4 Conclusions

The paper develops a triple-exposure color PIV procedure to reconstruct instantaneous pressure and the validation of

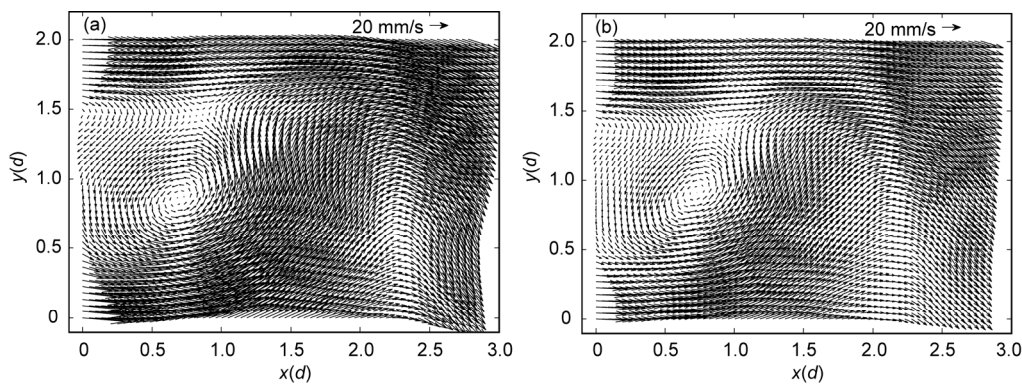


**Figure 12** Experimental velocity fields for two methods (from the *R, G* layer). (a) TE-CPIV with intensity correction; (b) classical PIV.

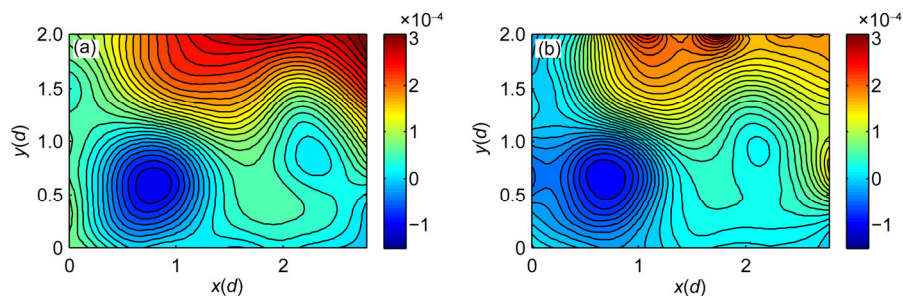


**Figure 13** (Color online) Experimental pressure field for two methods. (a) TE-CPIV; (b) classical PIV.

its feasibility. Three different color illuminations ( $R$ ,  $G$ , and  $B$ ) are produced in a time sequence. Particle images at different instants are captured in one exposure using a color digital SLR camera. An algorithm of contamination correction is performed on the color image, after which the color image is separated into three different color layers. Standard cross-correlation in the classical PIV method can be used to obtain two velocity fields from separated color layers. Finally, a pressure field can be reconstructed from the two velocity fields. This procedure was assessed by two experiments. One was a solid body rotation flow and the other was a cylinder wake flow. The main conclusions are summarized as follows:

(1) Each color illumination (three primary colors) can cause contaminated intensity on other color layers for the SLR camera recording system, which must be corrected for velocity deduction. This imaging characteristic is investigated by taking a calibration image for each color light and performing a statistical analysis on the intensity of the different raw color layers. Calibration functions could be obtained by a second-order polynomial fitting of the statistical result, which would be further coupled together to generate contamination correction equations. After solving the correction equations, new color layers are generated using corrected intensity, which are used for velocity and pressure determination.

(2) The instantaneous pressure field was successfully reconstructed using the TE-CPIV method. Both experiments, the solid body rotation flow and the cylinder flow, show that the reconstructed pressure has a reasonable accuracy.

(3) The TE-CPIV setup is easily achievable with simple and low-cost commercial devices, such as using a projector as the light source and a color SLR camera as the imaging system. Meanwhile, the setup can be improved with other advanced devices. With three or more color SLR cameras, the TE-CPIV method has the potential to be extended into three-dimensional flow measurement.

*This work was supported by the National Natural Science Foundation of China (Grant Nos. 11472030, 11327202 & 11490552) and the Fundamental Research Funds for the Central Universities (Grant No. YWF-16-JCTD-A-05).*

- 1 Van Oudheusden B W. PIV-based pressure measurement. *Meas Sci Tech*, 2013, 24: 390–392
- 2 Sridhar G, Katz J. Drag and lift forces on microscopic bubbles entrained by a vortex. *Phys Fluids*, 1995, 7: 389–399
- 3 Chang K. A multi-pulsed PTV technique for acceleration measurement. In: *Proceedings of International Workshop on PIV'99-Santa Barbara*, 3rd. Santa Barbara, 1999
- 4 Liu X, Katz J. Instantaneous pressure and material acceleration measurements using a four-exposure PIV system. *Exp Fluids*, 2006, 41: 227–240
- 5 Jaw S Y, Sheen J J, Hwang R. Development and application of an alternating-color micro-PIV system. In: *Proceedings of ASME 2014 International Mechanical Engineering Congress and Exposition, IMECE 2014*. American Society of Mechanical Engineers (ASME), 2014
- 6 Charonko J J, Antoine E, Vlachos P P. Multispectral processing for color particle image velocimetry. *Microfluid Nanofluid*, 2014, 17: 729–743
- 7 McGregor T J, Spence D J, Coutts D W. Laser-based volumetric colour-coded three-dimensional particle velocimetry. *Opt Lasers Eng*, 2007, 45: 882–889
- 8 McGregor T J, Spence D J, Coutts D W. Laser-based volumetric flow visualization by digital color imaging of a spectrally coded volume. *Rev Sci Instrum*, 2008, 79: 013710
- 9 Ruck B. Colour-coded tomography in fluid mechanics. *Opt Lasers Eng*, 2011, 43: 375–380
- 10 Cenedese A, Pagliarunga A. A new technique for the determination of the third velocity component with PIV. *Exp Fluids*, 1989, 8: 228–230
- 11 Pick S, Lehmann F O. Stereoscopic PIV on multiple color-coded light sheets and its application to axial flow in flapping robotic insect wings. *Exp Fluids*, 2009, 47: 1009–1023
- 12 Brückner C. 3-D PIV via spatial correlation in a color-coded light-sheet. *Exp Fluids*, 1996, 21: 312–314
- 13 Murai Y, Yumoto T, Oishi Y, et al. Color tomographic PIV improved by removal of color contamination. In: *Proceedings of 10th International Symposium on Particle Image Velocimetry*. Delft, Delft University of Technology, Faculty of Mechanical, Maritime and Materials Engineering, and Faculty of Aerospace Engineering, 2013
- 14 Cenedese A, Romano G P. Comparison between classical and three-color PIV in a wake flow. *J Flow Visual Image Process*, 1993, 1: 371–384
- 15 Funatani S, Takeda T, Toriyama K. High-resolution three-color PIV technique using a digital SLR camera. *J Flow Visual Image Process*, 2013, 20: 35–45
- 16 Jaw S Y, Hwang R R, Shyu K L. Development and application of LED illumination color PIV. In: *Proceedings of 2006 ASME Joint US-European Fluids Engineering Division Summer Meeting*. Miami, 2006
- 17 Jaw S Y, Wu J L. Alternating color image anemometry and its application. *J Flow Visual Image Process*, 2000, 7: 189–205
- 18 McPhail M J, Fontaine A A, Krane M H, et al. Correcting for color crosstalk and chromatic aberration in multicolor particle shadow velocimetry. *Meas Sci Tech*, 2015, 26: 25302
- 19 McGregor T, Jeffries B, Spence D, et al. Three dimensional particle image velocimetry using colour coded light sheets. In: *Proceedings of Fourth Australian Conference on Laser Diagnostics in Fluid Mechanics and Combustion*. The University of Adelaide, South Australia, 2005
- 20 Borowsky J, Wei T. Simultaneous velocimetry/accelerometry measurements in a turbulent two-phase pipe flow. *Exp Fluids*, 2006, 41: 13–20
- 21 Dong P, Hsu T Y, Atsavapranee P, et al. Digital particle image accelerometry. *Exp Fluids*, 2001, 30: 626–632
- 22 Greated C, Skyner D, Bruce T. Particle image velocimetry (PIV) in the coastal engineering laboratory. *Coastal Eng Proc*, 1992, 1: 212–225
- 23 Hirakawa K, Wolfe P J. Spatio-spectral color filter array design for optimal image recovery. *IEEE Trans Image Process*, 2008, 17: 1876–1890
- 24 Chen T. A study of spatial color interpolation algorithms for single-detector digital cameras. *Information System Laboratory Department of Electrical Engineering, Stanford University*, 1999
- 25 Raffel M, Willert C E, Kompenhans J. *Particle Image Velocimetry: A Practical Guide*. Berlin Heidelberg: Springer, 2013
- 26 Koschatzky V, Moore P, Westerweel J, et al. High speed PIV applied to aerodynamic noise investigation. *Exp Fluids*, 2011, 50: 863–876
- 27 Thomas F O, Liu X. An experimental investigation of symmetric and

- asymmetric turbulent wake development in pressure gradient. *Phys Fluids*, 2004, 16: 1725–1745
- 28 Van Oudheusden B W, Scarano F, Roosenboom E W M, et al. Evaluation of integral forces and pressure fields from planar velocimetry data for incompressible and compressible flows. *Exp Fluids*, 2007, 43: 153–162
- 29 Christensen K T, Adrian R J. Measurement of instantaneous Eulerian acceleration fields by particle image accelerometry: Method and accuracy. *Exp Fluids*, 2002, 33: 759–769
- 30 De Kat R, van Oudheusden B W. Instantaneous planar pressure determination from PIV in turbulent flow. *Exp Fluids*, 2012, 52: 1089–1106
- 31 Violato D, Moore P, Scarano F. Lagrangian and Eulerian pressure field evaluation of rod-airfoil flow from time-resolved tomographic PIV. *Exp Fluids*, 2011, 50: 1057–1070
- 32 Wang Z, Gao Q, Wang C, et al. An irrotation correction on pressure gradient and orthogonal-path integration for PIV-based pressure reconstruction. *Exp J Fluids*, 2016, 57: 1–16
- 33 Scarano F. Iterative image deformation methods in PIV. *Meas Sci Tech*, 2002, 13: R1
- 34 Prasad A, Adrian R, Landreth C, et al. Effect of resolution on the speed and accuracy of particle image velocimetry interrogation. *Exp Fluids*, 1992, 13: 105–116
- 35 Halvorsen K. Bias compensated least squares estimate of the center of rotation. *J Biomech*, 2003, 36: 999–1008
- 36 McKenna S, McGillis W. Performance of digital image velocimetry processing techniques. *Exp Fluids*, 2002, 32: 106–115
- 37 Huang H, Dabiri D, Gharib M. On errors of digital particle image velocimetry. *Meas Sci Tech*, 1997, 8: 1427
- 38 Gui L, Wereley S. A correlation-based continuous window-shift technique to reduce the peak-locking effect in digital PIV image evaluation. *Exp Fluids*, 2002, 32: 506–517
- 39 Garcia D. A fast all-in-one method for automated post-processing of PIV data. *Exp Fluids*, 2011, 50: 1247–1259
- 40 Wang C, Gao Q, Wei R, et al. Divergence-free smoothing for 3D-3C PIV data. In: *Proceedings of 4th International Conference on Experimental Fluid Mechanics*. Beijing, 2014
- 41 Pan C, Wang H, Wang J. Phase identification of quasi-periodic flow measured by particle image velocimetry with a low sampling rate. *Meas Sci Tech*, 2013, 24: 055305
- 42 Berkooz G, Holmes P, Lumley J L. The proper orthogonal decomposition in the analysis of turbulent flows. *Ann Rev Fluid Mech*, 1993, 25: 539–575
- 43 Stucky M J, Nino E, Gajdeczko B, et al. Two-color particle image velocimetry technique for an internal combustion engine. *Exp Therm Fluid Sci*, 1994, 8: 305–314
- 44 Bendicks C, Tarlet D, Roloff C, et al. Improved 3-D particle tracking velocimetry with colored particles. *J Signal Inf Proc*, 2011, 2: 59–71
- 45 Watamura T, Tasaka Y, Murai Y. LCD-projector-based 3D color PTV. *Exp Therm Fluid Sci*, 2013, 47: 68–80